

Lithospheric structure and tectonics at Isidis Planitia, Mars

J. Andreas Ritzer*, Steven A. Hauck, II

Department of Geological Sciences, Case Western Reserve University, 112 A.W. Smith Bldg., 10900 Euclid Ave, Cleveland, OH 44106-7216, United States

ARTICLE INFO

Article history:

Received 2 May 2008

Revised 3 December 2008

Accepted 21 January 2009

Available online 13 February 2009

Keywords:

Mars

Tectonics

Geophysics

ABSTRACT

We characterize the lithospheric structure of Isidis Planitia on Mars by analyzing Mars Global Surveyor and Mars Odyssey gravity and topography data using a flexural model of a thin elastic shell including bending and membrane stresses. Isidis Planitia is a circular, relatively flat plain formed near the end of the Early Noachian, at the edge of the highlands–lowlands boundary and the site of a large free-air gravity anomaly, features consistent with modification and filling of an impact basin. Our results suggest that the bulk density of the fill material inside Isidis must be more than 2600 kg m^{-3} and higher densities are probable. A comparison of the faulting observed at Nili Fossae to the predicted zone of extensional strain northwest of Isidis constrains the thickness of the elastic lithosphere to be 100–180 km thick beneath the basin at the time of loading. We also find that loads outside of the basin play a significant role in the interpretation of the tectonics; simplified models tend to overestimate the lithospheric thickness. We place relatively narrow bounds on the thermal gradient ($3.4\text{--}6.5 \text{ K km}^{-1}$) and heat flux ($13.6\text{--}26 \text{ mW m}^{-2}$) at Isidis at the time of loading.

© 2009 Elsevier Inc. All rights reserved.

1. Introduction

Characterizing the lithosphere of Mars is an important step towards understanding the state of its surface and interior. The lithosphere, which is the outer, mechanically rigid shell of the planet, responds directly to loads imposed upon it. Observations of the response of planetary surfaces are inherently useful because they can provide constraints on the structure of the lithosphere and the applied loads. The structure of the lithosphere is especially important at Isidis Planitia as it lies directly on the boundary between the southern highlands, with its higher topography and thicker crust, and the adjacent lower and thinner northern plains. Leveraging recently acquired topography and gravity data for Mars (e.g., Smith et al., 1999a, 1999b, 2001; Lemoine et al., 2001; Tyler et al., 2001; Yuan et al., 2001; Konopliv et al., 2006) provides the opportunity to develop a better understanding of the lithosphere in this region as well as additional constraints on the history of lithospheric heat flow (e.g., Solomon and Head, 1990; Zuber et al., 2000; McGovern et al., 2002).

Gravity and topography data are important indicators of lateral variations in the properties of the crust (e.g., Phillips et al., 1973) and lithosphere of planetary bodies (Spohn et al., 2001). Techniques for analyzing the transfer function between gravity and topography, known as admittance, are commonly employed using models to estimate local lithospheric and crustal thicknesses (e.g., Forsyth, 1985; McGovern et al., 2002; Belleguic et al., 2005)

when these datasets are spectrally correlated in spatially localized regions. Admittance modeling techniques have been successful at providing estimates of the thickness of the lithosphere beneath major volcanoes, the rim of the Hellas basin, and other surface features on Mars (McGovern et al., 2002; Belleguic et al., 2005). While these models have been successful in several regions on Mars, gravity and topography data in the northern plains, including Isidis Planitia, tend to be uncorrelated, and hence previously used admittance modeling techniques are incapable of adequately modeling lithospheric flexure of this important part of the martian surface (McGovern et al., 2002). However, approaches for investigating the rigidity of the lithosphere at Isidis using forward flexural modeling techniques (Comer et al., 1985) as well as flexural modeling constrained by gravity and topography data (Banerdt, 1986; Searls et al., 2006) are more capable in this situation. Isidis is the only major basin on Mars ringed by distinct circumferential graben like those of some lunar mascons (Comer et al., 1979; McGovern et al., 2002) that are associated with flexure of the basin. Therefore, in addition to gravity and topography data, the locations of extensional faulting surrounding Isidis can be used as a further constraint on flexural models (Comer et al., 1985).

We analyze gravity and topography data, as well as the expression of circumferential faulting at Isidis in order to understand the lithospheric and crustal structure of the basin. First, we apply an extension of Banerdt's (1986) well-known flexural model in order to characterize the range of parameters capable of satisfying the gravity and topography data. Second, we compare the stresses predicted by our flexural model to the observed tectonics around Isidis to constrain estimates of the thickness of the elastic litho-

* Corresponding author.

E-mail address: jar36@case.edu (J.A. Ritzer).

to the southeast of Isidis. Both of these extensional tectonic features may have formed during the middle Noachian (Tanaka et al., 2005), which is distinctly younger than the early Noachian age estimate for basin formation (Tanaka et al., 2005). Within the basin are features that resemble compressional wrinkle ridges, consistent with mascon loading scenarios (Wichman and Schultz, 1989), though recent work suggests that these features may also be lava flow fronts (Ivanov and Head, 2003).

3. Approach

The structure of the near subsurface of Isidis is analyzed using a model for the deformation of a thin, elastic, spherical shell (e.g., Turcotte et al., 1981; Willemann and Turcotte, 1982; Banerdt, 1986; Phillips et al., 2001) constrained by the present-day geoid and topography. Variations in relief at the surface and internal density interfaces, such as at the crust–mantle boundary, as well as excess mantle buoyancy, lead to net loads on the lithosphere that result in deformation. Following the general approach of Banerdt (1986), both vertical and horizontal load components are included in the elastic shell deformation model that accounts for both elastic bending and membrane support of lithospheric loads.

We calculate the deformation of the lithosphere and the subsequent stress state resulting from the vertical load $q(\theta, \phi)$ and horizontal load potential $\Omega(\theta, \phi)$ as a function of colatitude, θ , and longitude, ϕ , in the spherical harmonic domain. We model the deformation using a typical assumption that a thin elastic shell (e.g., Turcotte et al., 1981) can approximate the lithosphere. Furthermore, we utilize the observed topography $H(\theta, \phi)$ and geoid height $G(\theta, \phi)$ as explicit constraints (Banerdt, 1986). The data (i.e., q, Ω, H, G , etc.) are represented by spherical harmonics on a surface

$$f(\theta, \phi) = \sum_{\ell=0}^{\infty} \sum_{m=-\ell}^{\ell} a_{\ell m} Y_{\ell}^m(\theta, \phi),$$

where ℓ is the harmonic degree, m is the harmonic order, $a_{\ell m}$ are the harmonic coefficients, and $Y_{\ell}^m(\theta, \phi)$ are the spherical harmonics. We represent each geophysical parameter by these coefficients and perform the equations relating them on a degree-by-degree basis (e.g., Banerdt, 1986).

We use global representations of the Mars Global Surveyor (MGS) Mars Orbiter Laser Altimeter (MOLA) topography (Smith et al., 1999b, 2001) and MGS and Mars Odyssey derived gravitational potential field (Smith et al., 1999a; Tyler et al., 2001; Lemoine et al., 2001; Yuan et al., 2001; Konopliv et al., 2006) data, using spherical harmonic gravity model MGS95J which are expanded to degree and order 95, but truncated at degree and order 70 as noise in the data are equal to the signal for higher degree terms (Konopliv et al., 2006). We extend Banerdt's (1986) model for the deformation of a thin elastic shell, which relates these data to the inferred displacement and stresses. The model setup, illustrated in Fig. 3, assumes that when the Isidis basin formed it had an initial degree of compensation relating relief on the crust–mantle interface δc , known as the mocho, to the surface expression of the basin by $\delta c = C_f \rho_c / \Delta \rho O_b$, where C_f is a constant degree of compensation (0 = no compensation, 1 = complete Airy isostatic compensation), ρ_c is an assumed average global crustal density, O_b is the pre-loading basin shape, and $\Delta \rho = \rho_m - \rho_c$, where ρ_m is the average global mantle density. We extend Banerdt's original model by also considering the possibility of an additional density interface due to subsequent filling of the basin with a material of density ρ_F , to a thickness of F (see also Searls et al., 2006 for a similar formulation). The non-isostatic loads within the basin deflect the lithosphere by an amount w that is consistent with the observed topography H and geoid G . The thickness of fill, F , is:

$$F = H - w - O_b \quad (1)$$

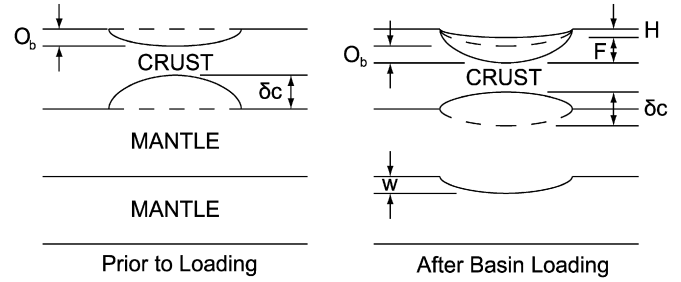


Fig. 3. Diagram of loading model. Parameters are O_b , original basin shape; δc , crustal thickness anomaly; H , observed topography; F , thickness of fill material; w , vertical displacement. All values are defined positive upwards except w .

as present-day topography, H , is the sum of the pre-loading basin shape, O_b , the thickness of the fill material F , and the deflection of the lithosphere w . The gravity anomaly observed within Isidis is likely due to some combination of a non-isostatic compensation state of the basin prior to infill and the excess mass of the fill in the basin (Neumann et al., 2004).

The additional density interface introduces more terms to the standard formulation of Banerdt (1986). The relation for net vertical load is

$$q = g_a [\rho_F F + \rho_c (w - G) + \rho_c O_b] + g_c [\Delta \rho (w - G_c) - C_f \rho_c O_b], \quad (2)$$

where g_a is the acceleration of gravity at the surface, g_c is the acceleration of gravity on the Moho, and G_c is the geoid height at the Moho. Previous studies using a Banerdt-type model (e.g., Banerdt, 1986; Searls et al., 2006) do not explicitly include the variation of gravity with depth; g_a and g_c approximate this effect in manner similar to Banerdt and Golombek (2000). The geoid height at the surface is

$$G = \frac{3}{\bar{\rho}(2\ell + 1)} \left\{ \rho_F F + \rho_c (O_b + w) + [\Delta \rho w - C_f \rho_c O_b] \left(\frac{R - c}{R} \right)^{\ell + 2} \right\}, \quad (3)$$

where $\bar{\rho}$ is the mean bulk density of Mars and R is the radius to the mid-plane of the elastic shell. Similarly, the geoid height at the base of the crust is

$$G_c = \frac{3}{\bar{\rho}(2\ell + 1)} \left\{ \rho_F F \left(\frac{R - c}{R} \right)^{\ell} + \rho_c (O_b + w) \left(\frac{R - c}{R} \right)^{\ell} + [\Delta \rho w - C_f \rho_c O_b] \right\}. \quad (4)$$

With the new density interface, the horizontal load potential is then

$$\Omega = \frac{\nu}{1 - \nu} \rho_F g_a L \frac{F}{R} - \frac{\nu}{1 - \nu} C_f \rho_c g_m (L - c) \frac{O_b}{R} + \frac{\nu}{1 - \nu} \rho_c g_a c \frac{O_b}{R} + [\rho_c g_m c + \rho_m g_c (L - c)] \frac{w}{R} \quad (5)$$

where L is the thickness of the elastic lithosphere and c is the mean crustal thickness of Mars. Banerdt (1986) derives the vertical displacement produced by both the vertical load and the horizontal load potential:

$$w = \alpha q + \gamma \Omega, \quad (6)$$

where

$$\alpha = -\frac{R^4}{D} \frac{f_{\ell} + 1 - \nu}{f_{\ell}^3 + 4f_{\ell}^2 + \psi(1 - \nu^2)(f_{\ell} + 2)}, \quad (7)$$

$D = EL^3/12(1 - \nu^2)$ is the flexural rigidity, E is the Young's modulus, $f_\ell = -\ell(\ell + 1)$, $\psi = 12(R/L)^2$, and

$$\gamma = \alpha \frac{f_\ell(1 + \nu - f_\ell/\psi)}{f_\ell + 1 - \nu}. \quad (8)$$

We solve Eqs. (1)–(6) simultaneously, which allows us to infer the structure of the basin for assumed global parameter values as well as determine the corresponding elastic deformation of the lithosphere.

The addition of the intracrustal density interface between the basin fill material and average crust is an important step toward quantifying the relationship between the amount of moho relief and basin fill material that are consistent with the observed gravity and topography data. However, the additional density interface also introduces more parameters to the problem; in particular, we must make *a priori* assumptions about the density of the fill material in any given model. Furthermore, we must also calculate the thickness of the fill material and the depth of the original basin. Though the intracrustal interface widens the potential parameter space, the additional generality of the extended formulation is consistent with the geological context of Isidis Planitia.

4. Results

Our primary goal is to understand the range of lithospheric thicknesses and basin crustal properties that are consistent with observations. Towards this goal, we explore a broad range of plausible model parameters (e.g., L , c , ρ_F , ρ_c , etc.) and potential tradeoffs among parameters (Table 1 lists variable parameters varied and Table 2 constant parameters applicable to all models). The basic approach is to leverage a comprehensive exploration of the model's plausible parameter space with two additional geologic constraints. First, we make the reasonable assumption that there is no exposed mantle within the Isidis basin. Second, calculation of the deformation-induced stress field near the basin provides the opportunity to assess whether individual models are consistent with the existence, style, and orientation of faulting, particularly at Nili and Amenthes Fossae. The latter is particularly useful for constraining estimates of elastic lithospheric thickness. Combined, this approach affords the opportunity to investigate the range of, and tradeoffs among, lithospheric and crustal properties that are physically consistent with the gravity and topography data as well as geological constraints.

4.1. Globally-constrained flexural models

We calculate a large suite of global flexural models explicitly constrained by present-day gravity and topography in order to understand lithospheric and crustal properties near Isidis Planitia. By considering a broad range of values for the mean crustal thickness c , elastic lithospheric thickness L , mean density of fill ρ_F , compensation factor C_f , and mean crustal density ρ_c (see Table 1) we are able to calculate how fill thickness F , crustal thickness local to Isidis $c_l = c - O_b - \delta c - F$ (at a time post-impact and prior to infilling), original basin shape O_b , and displacement w vary with these parameters in order to produce the observed gravity and topography. Though these calculations are inherently non-unique, by applying the reasonable constraint that $c_l > 0$ we can considerably limit the range of valid models.

The origin of the majority of material filling Isidis, and indeed the northern plains, is unclear, though the presence of Syrtis Major to the west suggests that significant volcanic deposits are possible (e.g., Tornabene et al., 2008). Large values for the density of the basin fill material (ρ_F) would be consistent with such an idea. Fig. 4 illustrates how fill density varies with lithospheric thickness (L) and mean global crustal thickness (c); each line is a contour of

Table 1

Range of model input parameters used in this study. Nominal values are best estimates from Wieczorek and Zuber (2004) as well as those values which matched all of our constraining criteria, and were used during analysis when not varied. All combinations of these values at resolution were modeled.

Input parameter	Range	Nominal	Resolution
c	30–90 km	50 km	10 km
L	50–220 km	120 km	10 km
ρ_c	2600–3400 kg m ⁻³	2900 kg m ⁻³	100 kg m ⁻³
ρ_F	2600–3400 kg m ⁻³	3100 kg m ⁻³	100 kg m ⁻³
C_f	0.2–1.6	1.0	0.1

Table 2

Parameters common to all models.

Constant	Value
ρ_m	3500 kg m ⁻³
g	3.71 m s ⁻²
R	3389.5 km
E	1.0×10^{11} Pa
ν	0.25

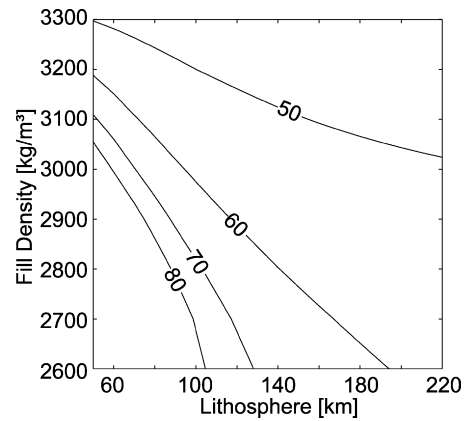


Fig. 4. Limits on fill density as a function of lithospheric and crustal thickness. Local crustal thickness is defined as the depth of crust after impact and before infilling. The local crustal thickness is positive above these lines and negative below. Nominal values were used for all parameters not shown, as given by Table 1. Numbers on contours indicate the value of the global crustal thickness c in kilometers.

zero local crustal thickness (c_l) for a given value of c . The models in the parameter space above the surface defined by these contours have a positive local crustal thickness, while those below have negative crustal thickness; therefore, those models above these lines are permissible. Assuming that $c = 50$ km (Wieczorek and Zuber, 2004) implies a $\rho_F > 3000$ kg m⁻³, however, based on an analysis of geoid to topography ratios and a comprehensive survey of estimates in the literature these authors found that the most robust estimate of uncertainty in the mean global crustal thickness is ± 12 km. While a crustal thickness less than 50 km would imply a well-constrained, large value for the density of the fill material an increase of even 10 km in crustal thickness leads to an unconstrained value for ρ_F for an average crustal density of 2900 kg m⁻³.

A more conservative approach recognizes that while exhumation of the mantle by the Isidis-forming impact may be possible, basin infilling could obscure the mantle. Therefore, in Fig. 5 we include the fill material as a component of the local crustal thickness, and apply the constraint that it cannot be negative. These results show that a robust estimate of the minimum fill density is not feasible without knowledge of the depth of fill.

Another factor that influences our understanding of the crust and lithosphere at Isidis is the initial state of compensation of the basin (Fig. 6). The state of compensation of the Isidis basin

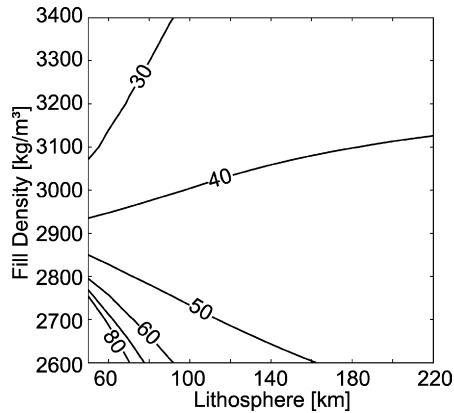


Fig. 5. Limits on fill density as a function of lithospheric and crustal thickness. Local crustal thickness is defined here as the crust present before fill plus the fill. Local crustal thickness is positive above these lines and negative below these lines. Nominal values were used for all parameters not shown, as given by Table 1. Numbers on contours indicate the value of the global crustal thickness c in kilometers.

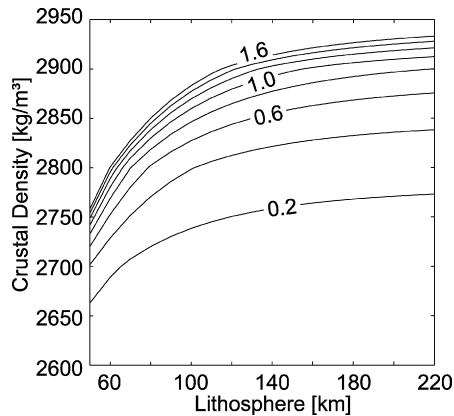


Fig. 6. Maximum crustal density as a function of lithospheric thickness and compensation factor. Local crustal thickness is negative above these lines and positive below. Nominal values were used for all parameters not shown, as given by Table 1. Numbers on contours indicate the value used for compensation factor C_f .

was varied between an under-compensation of $C_f = 0.2$ and an over-compensation of $C_f = 1.6$. The maximum value of $C_f = 1.6$ is consistent with the end-member assumption that the gravity anomaly can be explained entirely by super-isostatic relief along the Moho (Neumann et al., 2004). The clearest implication of the role of C_f is that the maximum possible mean global crustal density ρ_c increases as C_f increases; the same is true, but to a lesser extent for increasing lithospheric thickness. The variation with C_f is also non-linear as the relative change in ρ_c becomes smaller as the compensation factor increases. The maximum mean crustal density only varies by about 12% through a large range of compensation states for the nominal crustal thickness of 50 km.

4.2. Tectonic constraints

The distinct extensional tectonic features circumferential to the Isidis basin (Fig. 1) provide an additional opportunity, one not afforded by other large basins on Mars, to constrain the lithospheric structure of the region at the time material was filling the basin's interior. The strength of the lithosphere is finite and the state of stress induced by loads on the lithosphere controls the locations and style of faulting. Therefore, at Isidis the wide range of lithospheric loading models that satisfy the gravity and topography data can be further constrained by requiring successful models to match the observed locations, style, and orientation of faulting surrounding the basin.

Table 3

Summary of Fig. 5 in (Freed et al., 2001) describing the regions of the faulting styles determined by Simpson's shape parameter.

A_ψ (deg)	Fault-style from shape parameter
0–30	Pure normal faulting
30–75	Strike-slip and normal
75–105	Pure strike-slip faulting
105–150	Strike-slip and thrust
150–180	Pure thrust faulting

The lithospheric stress field at the surface (i.e. vertical stress is zero) is determined from the amount of deformation (w) of the elastic lithosphere, the vertical load (q), and the horizontal load potential (Ω) (see Banerdt (1986, Appendix A) for details). From this stress field we estimate both where the magnitude of stress exceeds the strength of the lithosphere as well as the style and orientation of any predicted faulting. Movement along a fault is favored after reaching a minimum level of stress in the lithosphere. Barnett and Nimmo (2002) inferred that extensional faults on Mars greater than 150 km across, such as may exist within the Valles Marineris system, withstood over 100 MPa differential stress (i.e., the difference between the maximum and minimum principal stresses), while smaller faults are more similar to terrestrial faults and only require about 20 MPa. Nili Fossae's largest fault is ~ 37 km across (Fig. 1) consistent with a rock strength somewhere between the 20 MPa and 100 MPa limits for a reasonable minimum to initiate faulting near Isidis, though the exact differential stress required is poorly constrained.

In addition to the requirement that the stresses exceed the strength of the lithosphere in order for our models to predict faulting, it is also necessary to determine the predicted style and orientation of faulting for comparison with Nili and Amenethes Fossae. The most common method for predicting the style of faulting using stress directions is Anderson's faulting criteria (Anderson, 1905). These criteria predict one of three styles of faults: normal (extension), strike-slip (shear), or thrust (compression). Anderson's criteria result in discrete predictions of only the major style of faulting, however, mixed modes of faulting are common in nature (e.g., trans-tensional), and therefore these criteria do not adequately address the full range of observed styles of faulting. A continuous representation of the faulting criteria was developed by Simpson (1997) in order to help alleviate this problem, and has been used to better understand and resolve the strike-slip faulting paradox of mascon loading on the Earth's moon (Freed et al., 2001). The geometrically defined Simpson's shape parameter

$$A_\psi = \tan^{-1}[(\sigma_1 - \sigma_\phi)/\sqrt{3}(\sigma_2 - P)] \quad (9)$$

is a continuous metric that implicitly includes the possibility of mixed-mode faulting styles. The largest and smallest compressive principal stresses on the radial/vertical plane axisymmetric to the center of the basin are σ_1 and σ_2 , respectively, σ_ϕ is the circumferential principal stress, and $P = (\sigma_1 + \sigma_2 + \sigma_\phi)/3$ is hydrostatic pressure. The types of faulting styles predicted by the shape parameter (Table 3) are pure as well as transitional modes of faulting. Table 3 lists the criteria for mapping values of A_ψ to the style and orientation of faulting; we have adopted the modified criteria proposed by Freed et al. (2001) which are weighted away from strike-slip faulting compared to the original criteria of Simpson (1997). The modified criteria are based upon the practical implementation of Simpson's framework, which recognizes that in mixed modes of faulting the non strike-slip component (normal or thrust) tends to be the observable expression of the faulting from orbit unless the mixed-mode is dominantly strike-slip in style (Freed et al., 2001).

Using the presence of faults surrounding Isidis as a constraint on lithospheric structure requires that our models must meet both

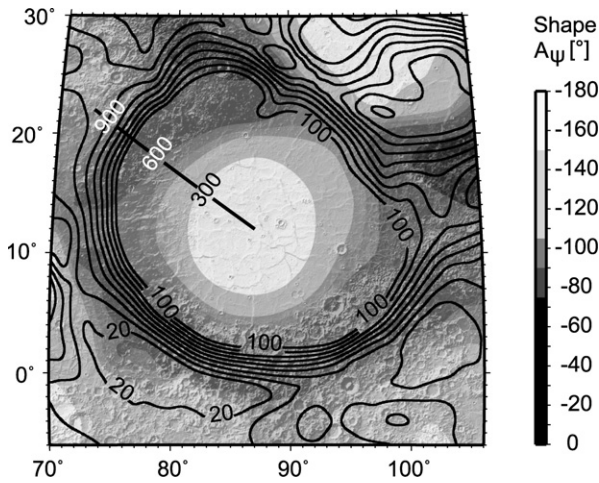


Fig. 7. Map of predicted faulting style based upon Simpson's shape parameter at Isidis for the nominal model. Differential stresses indicated by contour lines. The horizontal and vertical axes are east longitude and latitude, respectively. The contours show the stress differences from 20 to 100 MPa. Numbers in bold denote distance to the faults of Nili Fossae measured along the transect from the center of the figure to the top left. Lighter shading represents compressive, while darker shading indicates tensile faulting styles.

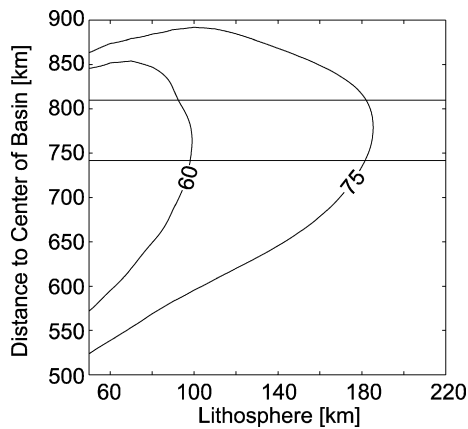


Fig. 8. Contours of shape parameter (shown in degrees), on a plot of distance to the center of the basin vs. lithospheric thickness. $A_\psi = 60^\circ$ is a lower bound for lithospheric thickness and $A_\psi = 75^\circ$ is an upper bound. The horizontal line at 810 km is the mean distance to the NB fault in Nili Fossae. The horizontal line at 740 km is the distance to fault NBa. The locations at which the contours cross the horizontal lines can be considered lower and upper bounds on lithospheric thickness.

criteria (sufficient stress magnitudes and the style) and orientation of faulting consistent with the modeled stress field must match the observed style of faulting at Nili and Amenthes Fossae. First, the amount of differential stress at the location of an observed fault must be greater than 20 MPa. Second, the Simpson's shape parameter must predict dominantly normal faulting circumferential to the basin ($0^\circ \leq A_\psi \leq 75^\circ$). An individual model is considered reasonable if both these criteria are met at the fault locations (e.g., Nili Fossae) and just as importantly a model must not predict inconsistent styles and orientations of faults (i.e. no circumferential graben inwards of the innermost faults).

We compare the calculated shape parameter to the locations of observed faulting (Fig. 7) to estimate limits on the thickness of the elastic lithosphere. Normal faulting is most definitively predicted when $A_\psi < 60^\circ$ and this then delineates the lower bound. Modeled values of $A_\psi < 60^\circ$ inward of the innermost faulting are not permissible, as that would imply normal faulting in the models closer to the interior of the basin than is observed. We use the innermost faults for comparison because they constrain where extensional faulting is observed. Stresses here are high enough that if

Table 4

Average distances from the center of Isidis Planitia to the innermost faults mapped at Nili and Amenthes Fossae. The ID's correspond to those seen in Fig. 1.

Fault ID name	Average distance (km)
NA	774
NB	809
NBa	742
AA	725

Table 5

Summary of thermal gradient and heat flux estimates as determined in McGovern et al. (2004). Ages are: Early Noachian—EN, Noachian—N, Hesperian—H, and Amazonian—A.

Feature	Surface age	L (km)	Thermal gradient (Km^{-1})	Heat flux (mWm^{-2})	Load density, P_l (kgm^{-3})
Olympus mons	A	>70	<8	<24	3150
Ascraeus mons	A	2–80	5–55	13–140	3250
Pavonis mons	A	<100	>5	>13	3250
Arsia mons	A	>20	<10	<28	3300
Alba Patera	A–H	38–65	5.5–16	16–40	2950
Elysium Rise	A–H	15–45	6–13	15–33	3250
Hebes Chasma	A–H	60–120	5–9	17–25	2100–2300
Candor Chasma	A–H	80–200	3–7.5	11–23	2200
Capri Chasma	A–H	>100	<7	<23	2500
Solis Planum	H	24–37	8–14	20–35	2900
Hellas south rim	H–N	20–31	10–16	25–40	2900
Hellas west rim	H–N	<20	>12	>30	2650
Hellas basin	N	<13	>14	>35	2750
Noachis Terra	N	<12	>20	>50	2800
Isidis Planitia	H	100–180	3.4–6.5	13.6–26	> 3100

compressional or strike-slip faulting were possible, it should be expressed in the landscape. We find the upper bound on lithospheric thickness using $A_\psi = 75^\circ$ which is the point where the dominant faulting style turns from normal faulting to strike-slip, therefore, the shape parameter cannot be above 75° outside the distance to the innermost fault otherwise the majority of Nili Fossae faulting would be predicted to be strike-slip. The example in Fig. 7 shows that in addition to a preference for normal faulting, stress differences are sufficient for faulting to occur at Nili and Amenthes Fossae, while other areas around the periphery have lower stresses.

In order to quantitatively assess our lithospheric flexure models we focus on comparing the stress magnitude and value of A_ψ along individual radial transects (e.g., the black diagonal line in Fig. 7) across Isidis that intersect the innermost normal faults. The transect in Fig. 7 is important because it intersects what we interpret to be the innermost visible normal fault associated with Nili Fossae, fault NBa (Fig. 1). As such, we have used the location of NBa as the limiting case of normal faulting for the majority of our analyses of flexurally induced tectonics at Isidis. Profiles of the value A_ψ along this transect were assembled for the entire range of lithospheric thicknesses (Fig. 8) in order to determine whether constraints can be put on the value of lithospheric thickness. The requirement that viable models match the style of faulting of the innermost faults implies that the intersection between the $A_\psi = 60^\circ$ contour and the distance to the innermost faults defines a lower bound for lithospheric thickness, while the intersection with the $A_\psi = 75^\circ$ contour defines an upper bound. The fault NB is 809 km from the center of the basin (Fig. 1 and Table 4), which gives a lower bound of ~ 100 km and an upper bound of ~ 180 km. However, these estimates are somewhat suspect because our constraint scheme fails in this scenario as the $A_\psi = 60^\circ$ intersection predicts compressive stress nearer to the basin than is seen, while the $A_\psi = 75^\circ$ intersection does not predict compressive stress outside of the fault. This result illustrates a potential pitfall of this technique, which is that the fault(s) used for the analysis must represent the innermost normal fault or the logic

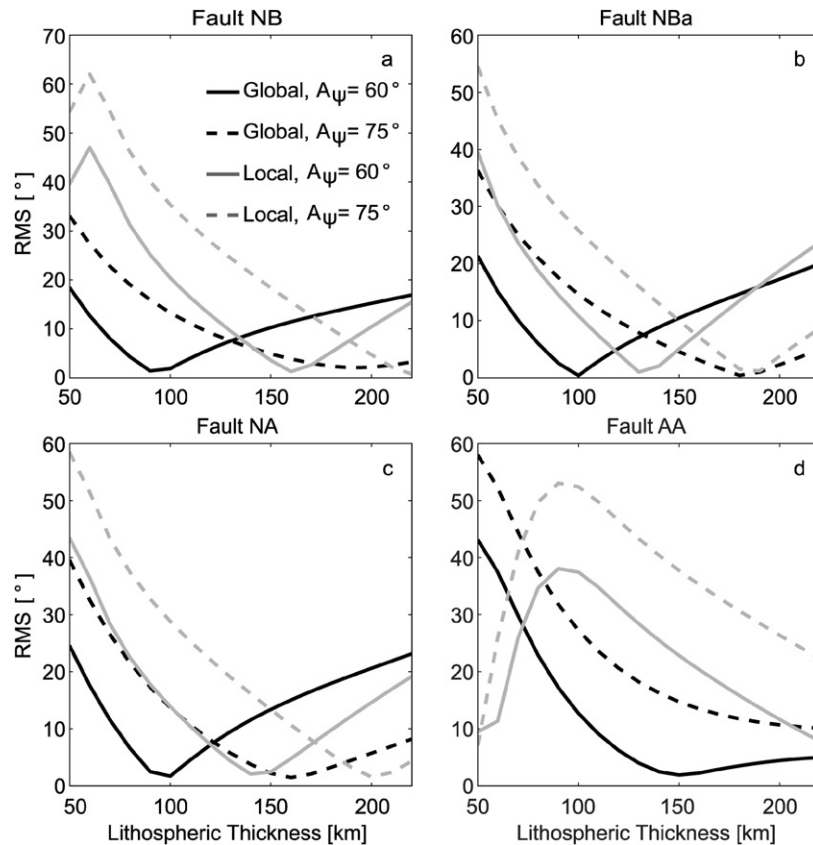


Fig. 9. RMS misfits between predicted and observed styles of faulting. Each panel corresponds to a particular mapped fault (Table 4). The solid lines are the misfit of shape parameter 60° and the dashed lines are for shape parameter 75° . The black lines are the misfits from the model using the global dataset, while grey lines are for the local models.

breaks down. Fortunately, both the aforementioned small fault NBa and the NB fault can be compared to each other directly as they lie on the same transect. The model predicts some unobserved extensional faults inwards of the observed fault(s) if the intersections of the distances with the contours of shape parameter are above the cusp of the contour. It is interesting to note that a model gives the location of the hidden fault NBa with almost precisely the same lithospheric thickness as the intersection with NB. We therefore assume that the bounds on lithospheric thickness are robust only if the locations of the faults are indeed the innermost bound of the faulting zone.

The shape parameter results from the radial transect in Figs. 7–9 demonstrate the utility of comparing the predicted faulting style with the observed location of the innermost normal faults at Isidis. By extending this idea to examine how shape parameter varies along the strike of a fault, we can develop a more robust determination of whether particular models are consistent with the observed faulting. We conducted a survey of the innermost faults of Nili and Amenthes Fossae at three different locations (Table 4). The RMS misfit between the shape parameter calculated by our models at those locations and the $A_\psi = 60^\circ$ and $A_\psi = 75^\circ$ contours provides a quantitative means for obtaining the best fit to these bounds (Fig. 9).

Nili Fossae is the more prominent of the two graben systems near Isidis, and has the most clearly defined faults. The faults mapped as NA, NB, and NBa all belong to the Nili Fossae system; however, as discussed above, the large NB fault does not lead to self-consistent interpretations, likely due to the presence of smaller, more inward faults, particularly NBa. The RMS misfit between the predicted and observed faulting location (Fig. 9) at NA and NBa are similar despite their azimuthal and radial separation. The consistency between the results for NA and NBa highlights

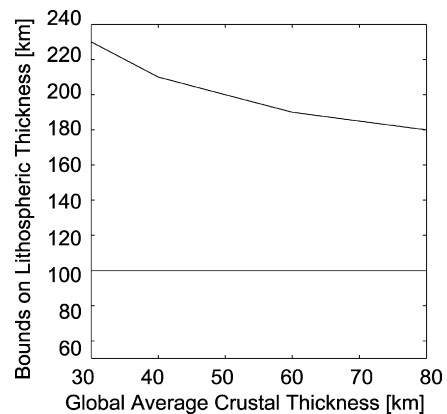


Fig. 10. Lower and upper bounds on the thickness of the elastic lithosphere. These bounds were determined by finding the lowest RMS misfits between predicted and observed styles of faulting at the NBa fault using the global model at various crustal thicknesses. See Figs. 8 and 9 for an explanation of the fitting method.

the spatial variability of the stress field as well as the potential strength of the approach of constraining the bounds on lithospheric thickness using observed faulting. For the nominal model parameters of Table 1, the lower bound on lithospheric thickness at Isidis is approximately 100 km, while the upper bound is ~ 180 km. Variations in the mean global crustal thickness have little effect on the lower bound of the lithospheric thickness (Fig. 10), however they lead to differences in the upper bound by $>20\%$.

Amenthes Fossae to the southeast of Isidis is a more subtle set of features with smaller and fewer visible extensional faults (Greeley and Guest, 1987; Tanaka et al., 2005). Our models also predict normal faulting in this area (Fig. 7); however, the interpre-

tation of these results is not as straightforward as at Nili Fossae. The RMS misfit at fault AA (Fig. 9) shows a much higher estimate for the bounds on lithospheric thickness. The RMS values at Amenthes are also higher than at Nili Fossae. Though somewhat speculative, this result suggests that there may be obscured faults further inward from fault AA, which would lead to an over-estimation of lithospheric thickness. However, a detailed survey of the area revealed no clear, smaller hidden faults, as is the case of fault NBa on the Nili Fossae side of the basin, which suggests that there may have been significant surface modification at Amenthes near the basin. It is also possible that the faults at Amenthes did not initiate at the same time as Nili Fossae, which would explain the difference in lithospheric thickness estimates.

4.3. Role of external loads on tectonics

A common approach for studying lithospheric flexure is to employ simplified load geometries that make for straightforward model calculations (e.g., Comer et al., 1979; Janes and Melosh, 1990; Comer et al., 1985). These studies also suffered from a relative lack of data that would justify a more precise modeling approach. Often these models use a single axisymmetric load shape that inevitably yields axisymmetric stress distributions and predictions of faulting rather than concentrated zones, such as observed along the periphery of Isidis. Though the lack of circumferentially continuous faulting may be the result of burial (e.g., near Syrtis) and erosion, the non-circumferential strike of the Nili Fossae graben belies that idea. Therefore, it is important to ask how much the inclusion (or exclusion) of loads, external to Isidis (or any other feature) affects our ability to infer lithospheric structure based upon the location of faulting.

Our basic approach to addressing the role of loads external to Isidis on regional tectonism is to compare the flexural response of the lithosphere near Isidis using the deformation model constrained by the global topography and gravity against an equivalent forward solution that models the response only due to loads within the impact basin. The comparison of these two models allows us to investigate the relative role of exterior loads in controlling the style and location of faulting.

In order to facilitate a direct comparison between the two types of models we isolated the relevant load components within the basin from the global models and used them as inputs for the forward models. Specifically, we extract the loads on the lithosphere at Isidis by localizing the size and shape of the basin, its fill material, and compensating relief along the moho from the globally constrained model. We use the local, forward model, with equivalent loading and flexure equations and identical flexural parameters, to determine the amount of deformation and lithospheric stress within and peripheral to the load that result from the loading internal to the basin.

The loads in the basin's interior were isolated using a spherical-cap localizing window in the spherical harmonic domain defined spectrally

$$J_{00} = \sqrt{4\pi}, \quad (10)$$

where J_{00} is the zeroth order term and

$$J_{\ell 0} = \sqrt{\frac{4\pi}{2\ell + 1} \frac{P_{\ell-1}(\cos \xi) - P_{\ell-1}(\cos \xi)}{P_0(\cos \xi) - P_1(\cos \xi)}}, \quad (11)$$

where $J_{\ell 0}$ are the zonal terms, P_{ℓ} are the associated Legendre polynomials of degree ℓ , and ξ is the angular radius of the desired window (Simons et al., 1997). The window is normalized to have a value of one within the window and zero outside. Because the localization window is defined purely by zonal harmonics, it is then rotated into a position centered on Isidis

and expanded into the spatial domain. We multiply the window with the global data, which localizes the data to the basin (Wieczorek and Simons, 2005) that are then transformed back into spherical harmonics up to degree and order 120 to minimize spectral leakage and ringing outside of the window. All of the operations on the data described above were accomplished using the freely available software archive SHTOOLS available at <http://www.ipgp.jussieu.fr/~wieczor/SHTOOLS/SHTOOLS.html>.

To generate the best possible comparison between the global and local loading models it is desirable to have loading conditions between the different model types be as similar as possible. At the center of the window (i.e. the basin) where the load magnitudes are greatest and contribute the most deformation, the localized loads are identical to loads from the global model and match well within the remainder of the localizing window (Figs. 11a–11b). Indeed, the window used here results in localized loads with maximum differences of less than 8% relative to the loads in the global model. There are discrepancies at the southern edge of the basin; however, these are due to the localizing window and especially the low magnitude of the signals here, which acts to magnify fractional differences. More importantly, the forward models based on these localized loads generally produce comparable topographic relief (Fig. 11c), gravity (Fig. 11d), and deflections with the global model, especially within the localized region of the basin, providing confidence in our approach.

The most readily apparent differences between the two models are the azimuthal variations of the stresses (Fig. 12c). The global model that includes external loads predicts circumferential extensional stresses concentrated near the locations of graben observed on the surface (Fig. 12a). The localized model, however, does not produce any significant azimuthal variations in stress (Fig. 12b). Therefore, variations in loading inside the basin do not substantially contribute to the azimuthal variations seen in the global model, or to the observed tectonics. The radial variations of stresses (Fig. 12c) from the center of the load are used to compare our models to observed conditions on the surface (Fig. 7) and the RMS misfit between these two distributions suggests a difference between the global and localized models (Fig. 9), where the localized models consistently predict larger values for the lithospheric thickness relative to the global model at each fault investigated. Moreover, the shape of the RMS curve for the localized model at fault AA is inconsistent with the global model. Therefore, the simplified local models do not fully characterize the faulting observed and consistently over-predict the estimates of lithospheric thickness at the time of Isidis Planitia's loading.

5. Discussion

5.1. Globally-constrained flexure models

The inversion of topography and gravity was constrained by the assumption that there should be a positive crustal thickness beneath the basin immediately after impact. Negative crustal thickness as defined in our model, would imply that excavation of the entire crust at Isidis Planitia upon impact is insufficient to account for the gravity signal observed. Models with negative crustal thickness necessitate excavation of a portion of the mantle or a reduction in local mantle density in concert with removal of the crust. We cannot rule out excavation of the mantle at the time of impact; however, the likelihood of a localized region of low-density mantle coincident with the placement of the basin is very low. While assuming that the local crustal thickness beneath Isidis at impact should be greater than zero is a logically sound constraint, it is not strictly testable with available observations. A more robust observation is that no mantle material has been detected at the surface inside Isidis, which suggests that the more conservative constraint

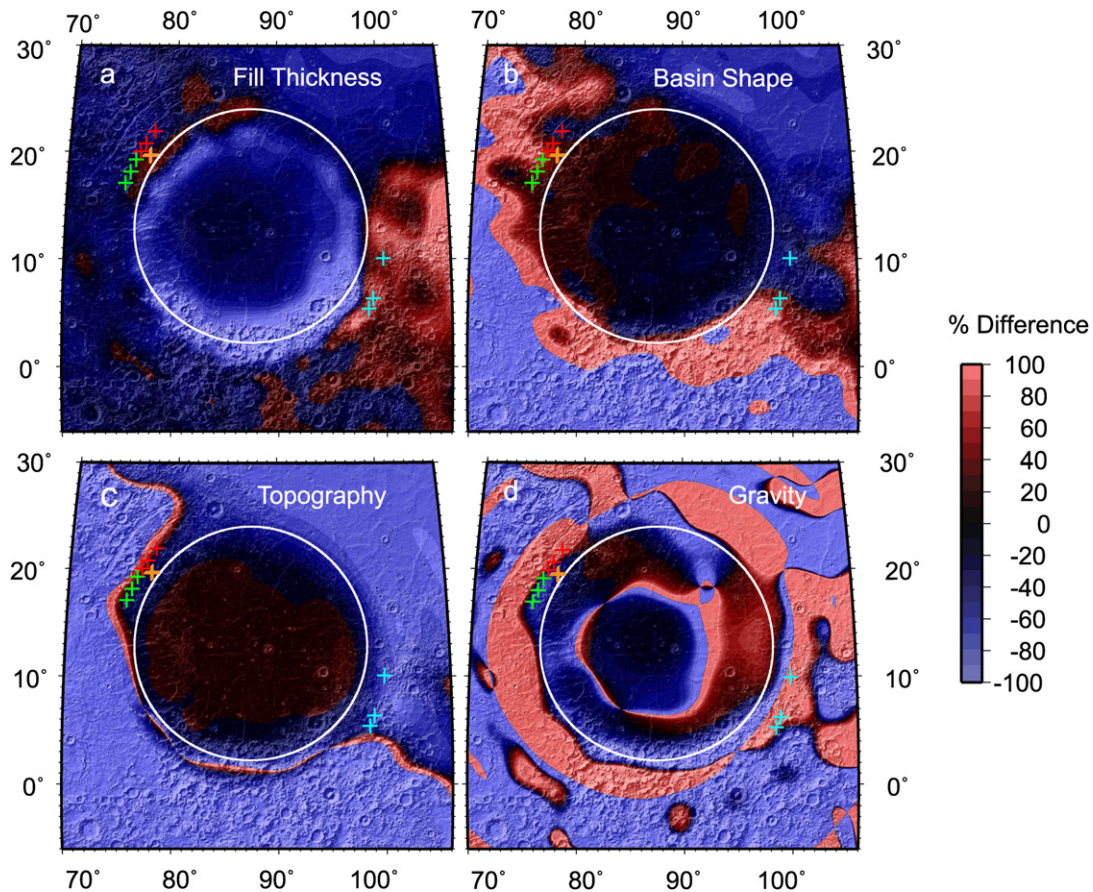


Fig. 11. Differences between the maps produced by the inverse model, and the maps used as input for the forward model. The white circle is the extent of the localizing window. The crosses indicate the locations of points used to represent individual faults around Isidis: magenta is fault NA, yellow is NB, orange is NBA, and white is AA (Table 4).

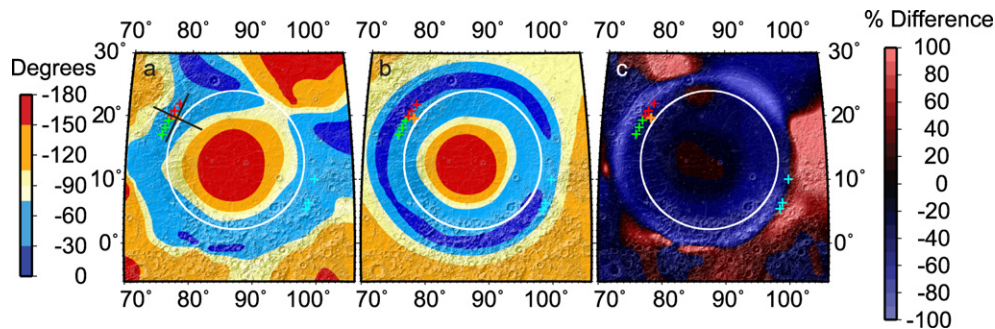


Fig. 12. The left two maps (a) and (b) show the predicted faulting style determined through shape parameter. Figure (a) is from the global model, while (b) is from the local model. (c) shows the difference between the two models for the nominal case. The black cross in (a) shows the directions of the principal stresses in an extensional regime where the largest stress is perpendicular to the observed graben.

is to limit acceptable models to those with a positive local crustal thickness at present.

The density of the fill material in the basin is more consistent with a value greater than 2900 kg m^{-3} , rather than lower, as more models that are reasonable exist with fill densities greater than this value rather than less. A mean global crustal thickness of 50 km (Wieczorek and Zuber, 2004) coupled with the upper bound we determined for the elastic lithospheric thickness ($L = 180 \text{ km}$) results in a fill density greater than 3050 kg m^{-3} (Figs. 4 and 5). This result implies that materials found within Isidis have a significant igneous component. The basin's proximity to the Syrtis Major volcanic province just west of the basin supports this interpretation, as it is a prime source region for an olivine-rich volcanic unit at least 800 m thick (Tornabene et al., 2008) on the western

edge of the basin. Kiefer (2004) estimated a surface material density in the Nili Fossae region similar to the Chassigny meteorite, which has a grain density of 3590 kg m^{-3} , and could contribute to a higher fill density in the basin. Furthermore, Kiefer (2004) found that Nili and Meroe Patera have a Nakhla-like density of 3290 kg m^{-3} , suggesting that the material flowing from the Syrtis region may be high-density lava flows. Both the volcanic sources and deposits in close proximity to the basin lend credence to the idea of a relatively high bulk density fill. This does not rule out the possibility of lower density material being present at the basin, but suggests that any such material will be more scarce than the volcanics. However, here we estimate the bulk fill density leaving open the possibility of higher density volcanic deposits interlayered with lower density sedimentary deposits that accrued episod-

ically over time (e.g., Head et al., 2002; Ivanov and Head, 2003; Hiesinger and Head, 2004).

The inversion of gravity observations in our formulation depends on the first-order mass sheet approximation calculation of the geoid heights and does not take into account any finite amplitude effects due to relief on density interfaces (Wieczorek and Phillips, 1998). However, owing to the small dynamic range of the topography in the study area of this paper, the discrepancy introduced by this approximation of the gravity was less than 2% over the entire area and less than 1% at the center of the basin where the load is greatest. The effect of this assumption on our results is therefore minimal.

5.2. Tectonic constraints

The existence of tectonic features clearly associated with Isidis Planitia provides a potentially important additional constraint on the state of the lithosphere compared to other basins on Mars. Indeed, the tectonic features are critical to understanding the flexure and lithospheric thickness around Isidis, as other methods (e.g., previous admittance studies) are not capable given that the basin's gravity and topography are not correlated. Application of the observed tectonics as a constraint on flexural models is not entirely straightforward, however, as there is a broad region of faulting (e.g., Nili Fossae), the distribution of faulting varies azimuthally, and the timing of faulting across the region is unconstrained. Basin filling ostensibly occurred over a finite time interval during which the lithospheric thickness may have changed, a common challenge of elastic flexure models. Thickening of the lithosphere due to cooling tends to freeze-in flexure, though progressive cooling during loading leads to lithospheric flexure estimates slightly thicker than if there were no cooling (e.g., Albert and Phillips, 2000). Therefore, absent thermal rejuvenation of the lithosphere beneath Isidis our results represent reasonable effective lithospheric thicknesses from the time of major infilling. However, more sophisticated finite element modeling with an elasto-viscoplastic rheology will be important for unraveling the tradeoffs in load timing, cooling, and relaxation of the basin and the implications for faulting in the region.

5.3. Role of external loads on tectonics

An important aspect of modeling lithospheric flexure is adequately capturing the relevant loads; this issue is amplified when considering the orientations and style of tectonic features as a constraint. Indeed, Banerdt's (1986) flexural formulation includes the horizontal load potential (Ω) that, while a modest contributor to overall lithospheric deflections, is important for stress magnitudes and orientations. At Isidis Planitia, loads external to the basin play an important role in shaping flexurally induced tectonism in the region as demonstrated by the distinct differences between our globally constrained models and the localized forward models. Important contributions to these loads arise from the nearby Syrtis Major and Utopia Planitia; the global response of the lithosphere to the Tharsis Plateau (Phillips et al., 2001) may also play a small role. Azimuthal variations in the predicted stress-state can be explained by the presence of external loads located heterogeneously around the periphery of the basin. In the globally constrained models, the largest stresses tend to be concentrated between external loads such as Syrtis Major and Utopia Planitia (e.g., Nili Fossae). The variation in the radial direction is due to the loads external to the basin that reduce the zone over which deformation caused by Isidis occurs, hence concentrating their magnitude.

Compared with the previous work of Comer et al. (1985), who estimated a lower bound on the lithospheric thickness at Isidis Planitia of 120 km and determined a best fit of between 200 and

300 km using a simplified, forward, axisymmetric model, our results suggest tighter limits and relatively thinner values for the lithospheric thickness. However, consistent with the limited data available at the time, their model only considered surface mass loads rather than including crust-mantle relief or intra-crustal density interfaces. Furthermore, by implementing a constraint that models match both the style of faulting and a threshold stress for faulting our results indicate that simplified, local forward models tend to overestimate the lithospheric thickness compared to those that include loads external to the basin in the analysis. We see this overestimation while comparing our lower bound of 100 km to the 120 km lower bound of Comer et al. (1985) along with our upper bound of 180 km compared to the 200 to 300 km best-fit lithospheric thickness of Comer et al. (1985). Given differences in the data available and modeling approach, the modest differences in results are quite reasonable.

5.4. Thermal gradient and heat flux

An important rationale for estimating the thickness of the elastic lithosphere for a variety of geological terrains (e.g., McGovern et al., 2002) is that such determinations are an important step in investigating the thermal history of Mars. Using the well-established methodology of McNutt (1984), we have calculated ranges of potential thermal gradients at Isidis at the time of loading based upon our results for upper and lower limits on elastic thickness (L). Thermal gradients are determined by translating estimates of the thickness of the elastic lithosphere found using our model to the thickness of the mechanical lithosphere T_m . The mechanical lithosphere is defined to be the depth at which the lithosphere has no mechanical strength. We may approximate this depth as an isotherm between 550 °C and 600 °C depending on the assumed strain rate (10^{-16} – 10^{-17} s $^{-1}$) (McNutt, 1984). The best estimates of the thickness of the crust at Isidis are significantly smaller than those of its elastic lithosphere, which allows us to assume that the ductile strength of the lithosphere is limited by the creep strength of olivine (Goetze, 1978), the likely dominant mineral in the lithospheric mantle. The relationship between the thicknesses of the elastic and mechanical lithospheres depends on the curvature of the lithosphere (McNutt, 1984; Solomon and Head, 1990; McGovern et al., 2002); greater curvature produces a larger difference between the elastic and mechanical thicknesses of the lithosphere. By calculating the second derivative of the deflection of the shell in our models we find the curvature of the lithosphere surrounding Isidis in our models is rather small, between 2×10^{-9} and 9×10^{-9} m $^{-1}$, which allows us to assume that $L \approx T_m$. We calculate the thermal gradients by assuming the surface temperature to be 220 K (Kieffer et al., 1977). For an elastic lithospheric thickness of 100 km (our lower bound), the thermal gradient is 6–6.5 K km $^{-1}$, while for a thickness of 180 km (our upper bound), it is 3.4–3.6 K km $^{-1}$ (Table 5). Surface heat fluxes are estimated from these thermal gradients using $q = k \frac{\partial T}{\partial z}$, where k is the mean thermal conductivity, assumed to be 4.0 W m $^{-1}$ K $^{-1}$ which is consistent for mantle material (McGovern et al., 2002) since the amount of crust beneath Isidis is minimal. For an elastic lithospheric thickness of 100 km, the heat flux is 24–26 mW m $^{-2}$; for a thickness of 180 km, it is 13.6–14.4 mW m $^{-2}$ (Table 5). The heat flux and thermal gradient estimated at Isidis are consistent with the general decline of mantle heat flux through time (McGovern et al., 2002), however the values seen at Isidis are lower than the results of Hauck and Phillips (2002) which may suggest that Isidis is an area of anomalously low heat flow. The heat flux at Isidis compares with the present day values (Hauck and Phillips, 2002) for an elastic thickness of 100 km, however the heat flux calculated for our upper range of elastic thicknesses is lower than any heat flux in the nominal model of Hauck and Phillips (2002). We estimate the

thermal properties of Isidis for the time of flexure corresponding to the initiation of faulting in Nili and Amenthes Fossae, dated to be of Middle Noachian age (Tanaka et al., 2005). The surface units in Isidis are significantly younger than Noachian with ages ranging from the Late Hesperian to the Early Amazonian, clearly the fill seen at the surface of Isidis cannot be responsible for the majority of the flexure. This result is not surprising, as the surface units appear to be quite thin (Buczowski, 2007). When compared to the results of McGovern et al. (2002), the thermal estimates for Isidis Planitia agree with a surface age in the Late Hesperian or Early Amazonian. The discrepancy between the ages of the tectonics and the age of the surface units suggests that surface ages can only be used as a bound on the youngest age of any results. Thus, we must be cautious when ascribing any physical properties to the timing of a feature by using the surface age as a lower bound.

6. Conclusions

The analysis of the tectonics at Isidis in concert with gravity and topography data has proven useful in constraining the elastic lithosphere beneath Isidis to be between 100–180 km thick, which is smaller than the range proposed by Comer et al. (1985). The range of lithospheric thickness determined in this study have provided a relatively narrow estimate of the thermal gradient beneath Isidis ($3.4\text{--}6.5\text{ K km}^{-1}$), and the heat flux ($13.6\text{--}26\text{ mW m}^{-2}$) at its surface. The ranges of thermal properties given here are consistent with those estimated by McGovern et al. (2004) however the age of the surface units at Isidis cannot be the only time at which material was emplaced as the fill densities are generally too high to be sedimentary. In this study, we have inferred the majority of the fill inside Isidis to be of densities higher than crustal density, which is corroborated by the fact that there is a large effusive volcanic province directly adjacent to the basin. This suggests that the surface layer Ali, which is interpreted to be sedimentary, should be quite thin (e.g., Buczowski, 2007). The surface age of Isidis should thus, only be used as a youngest bound for the ages of the flexure.

Localized loads modeled in a forward sense compared to the inverse global models have demonstrated that loads outside the basin are important to interpretations of lithospheric flexure. Models that do not include the external loads tend to overestimate the lithospheric thickness beneath a feature.

The elastic model used in this study was useful for constraining properties of the basin at the time of loading, which may have occurred during the Middle Noachian, however, this limited model cannot simulate any relative timing of loading events. Further investigation of this basin using a more sophisticated model with a more realistic and time-dependent rheology is warranted.

Acknowledgments

We are grateful to Bruce Banerdt and Mark Wieczorek for sharing code utilized in developing this study. Comments by Patrick McGovern and an anonymous reviewer helped sharpen the manuscript. GMT (Generic Mapping Tools) by Wessel and Smith (1998) was used to generate several of the figures. Support for this project was provided by the NASA Mars Data Analysis Program through grant NNG04GJ08G.

References

Albert, R.A., Phillips, R.J., 2000. Paleoflexure. *Geophys. Res. Lett.* 27, 2385–2388.
 Anderson, E.M., 1905. The dynamics of faulting. *Trans. Edinburgh Geol. Soc.* 8, 387–402.
 Arkani-Hamed, J., 1998. The lunar mascons revisited. *J. Geophys. Res.* 103, 3709–3739.
 Banerdt, W.B., 1986. Support of long-wavelength loads on Venus and implications for internal structure. *J. Geophys. Res.* 91, 403–419.

Banerdt, W.B., Golombek, M.P., 2000. Tectonics of the Tharsis Region of Mars: Insights from MGS topography and gravity. *Lunar Planet. Sci.* 31. Abstract #2038.
 Barnett, D.N., Nimmo, F., 2002. Strength of faults on Mars from MOLA topography. *Icarus* 157, 34–42.
 Belleguic, V., Lognonne, P., Wieczorek, M., 2005. Constraints on the martian lithosphere from gravity and topography data. *J. Geophys. Res.* 110, doi:10.1029/2005JE002437. E11005.
 Booker, J.R., Kovach, R.L., Lu, L., 1970. Mascons and lunar gravity. *J. Geophys. Res.* 75, 6558–6564.
 Buczowski, D.L., 2007. Stealth quasi-circular depressions (sQCDs) in the northern lowlands of Mars. *J. Geophys. Res.* 112, doi:10.1029/2006JE002836. E09002.
 Christensen, P.R., Gorelick, N.S., Mehall, G.L., Murray, K.C., 2006. THEMIS Public Data Releases, Planetary Data System node, Arizona State University. <http://themis-data.asu.edu>.
 Comer, R.P., Solomon, S.C., Head, J.W., 1979. Elastic lithospheric thickness on the Moon from mare tectonic feature: A formal inversion. *Proc. Lunar Sci. Conf.* 10, 2441–2463.
 Comer, R.P., Solomon, S.C., Head, J.W., 1985. Mars: Thickness of the lithosphere from the tectonic response to volcanic loads. *Rev. Geophys.* 23, 61–92.
 Forsyth, D.W., 1985. Subsurface loading and estimates of the flexural rigidity of continental lithosphere. *J. Geophys. Res.* 90, 12623–12632.
 Freed, A.M., Melosh, H.J., Solomon, S.C., 2001. Tectonics of mascon loading: Resolution of the strike-slip faulting paradox. *J. Geophys. Res.* 106, 20603–20620, doi:10.1029/2000JE001347.
 Frey, H.V., 2006. Impact constraints on, and a chronology for, major events in early Mars history. *J. Geophys. Res.* 111, doi:10.1029/2005JE002449. E08S91.
 Goetze, C., 1978. The mechanisms of creep in olivine. *Philos. Trans. R. Soc. London A* 288, 99–119.
 Greeley, R., Guest, J., 1987. Geologic map of the eastern equatorial region of Mars. *U.S. Geol. Surv. Misc. Invest. Ser.*
 Hauck, S.A. II, Phillips, R.J., 2002. Thermal and crustal evolution of Mars. *J. Geophys. Res.* 107, doi:10.1029/2001JE001801.
 Head, J.W., Kreslavsky, M.A., Pratt, S., 2002. Northern lowlands of Mars: Evidence for widespread volcanic flooding and tectonic deformation in the Hesperian Period. *J. Geophys. Res.* 107, doi:10.1029/2000JE001445. 5003.
 Hiesinger, H., Head, J.W., 2004. The Syrtis Major volcanic province, Mars: Synthesis from Mars Global Surveyor data. *J. Geophys. Res.* 109, doi:10.1029/2003JE002143. E01004.
 Ivanov, M.A., Head, J.W., 2003. Syrtis Major and Isidis basin contact: Morphological and topographic characteristics of Syrtis Major lava flows and material of the Vastitas Borealis formation. *J. Geophys. Res.* 108, doi:10.1029/2002JE001994. 5063.
 Janes, D.M., Melosh, H.J., 1990. Tectonics of planetary loading: A general model and results. *J. Geophys. Res.* 95, 21345–21355.
 Kiefer, W.S., 2004. Gravity evidence for an extinct magma chamber beneath Syrtis Major, Mars: A look at the magmatic plumbing system. *Earth Planet. Sci. Lett.* 222, 349–361.
 Kieffer, H.H., Martin, T.Z., Peterfreund, A.R., Jakosky, B.M., Miner, E.D., Palluconi, F.D., 1977. Thermal and albedo mapping of Mars during the Viking primary mission. *J. Geophys. Res.* 82, 4249–4291.
 Konopliv, A.S., Yoder, C.F., Standish, E.M., Yuan, D., Sjogren, W.L., 2006. A global solution for the Mars static and seasonal gravity, Mars orientation, Phobos and Deimos masses, and Mars ephemeris. *Icarus* 182, 23–50.
 Lemoine, F.G., Smith, D.E., Rowlands, D.D., Zuber, M.T., Neumann, G.A., Chinn, D.S., Pavlis, D.E., 2001. An improved solution of the gravity field of Mars (GMM-2B) from Mars Global Surveyor. *J. Geophys. Res.* 106, 23359–23376, doi:10.1029/2000JE001426.
 McGovern, P.J., Solomon, S.C., Smith, D.E., Zuber, M.T., Simons, M., Wieczorek, M.A., Phillips, R.J., Neumann, G.A., Aharonson, O., Head, J.W., 2002. Localized gravity/topography admittance and correlation spectra on Mars: Implications for regional and global evolution. *J. Geophys. Res.* 107, 5136, doi:10.1029/2002JE001854.
 McGovern, P.J., Solomon, S.C., Smith, D.E., Zuber, M.T., Simons, M., Wieczorek, M.A., Phillips, R.J., Neumann, G.A., Aharonson, O., Head, J.W., 2004. Correction to “Localized gravity/topography admittance and correlation spectra on Mars: Implications for regional and global evolution”. *J. Geophys. Res.* 109, doi:10.1029/2004JE002286. E07007.
 McNutt, M.K., 1984. Lithospheric flexure and thermal anomalies. *J. Geophys. Res.* 89, 11180–11194.
 Neumann, G.A., Zuber, M.T., Smith, D.E., Lemoine, F.G., 1996. The lunar crust: Global signature and structure of major basins. *J. Geophys. Res.* 101, 16841–16864, doi:10.1029/96JE01246.
 Neumann, G.A., Zuber, M.T., Wieczorek, M.A., McGovern, P.J., Lemoine, F.G., Smith, D.E., 2004. Crustal structure of Mars from gravity and topography. *J. Geophys. Res.* 109, doi:10.1029/2004JE002262. E08002.
 Nimmo, F., 2002. Admittance estimates of mean crustal thickness and density at the martian hemispheric dichotomy. *J. Geophys. Res.* 107, doi:10.1029/2000JE001488. 5117.
 Phillips, R.J., Conel, E., Abbott, E.A., Sjogren, W.L., Morton, J.B., 1972. Mascons: Progress toward a unique solution for mass distribution. *J. Geophys. Res.* 77, 7106–7114.

- Phillips, R.J., Saunders, R.J., Conel, J.E., 1973. Mars: Crustal structure inferred from Bouguer gravity anomalies. *J. Geophys. Res.* 78, 4815–4820.
- Phillips, R.J., Zuber, M.T., Solomon, S.C., Golombek, M.P., Jakosky, B.M., Banerdt, W.B., Smith, D.E., Williams, R.M.E., Hynes, B.M., Aharonson, O., Hauck, S.A., 2001. Ancient geodynamics and global-scale hydrology on Mars. *Science* 291, 2587–2591.
- Potts, L.V., von Frese, R.R., Leftwich, T.E., Taylor, P.T., Shum, C.K., Li, R., 2004. Gravity-inferred crustal attributes of visible and buried impact basins on Mars. *J. Geophys. Res.* 109, doi:10.1029/2003JE002225. E09009.
- Searls, M.L., Banerdt, W.B., Phillips, R.J., 2006. Utopia and Hellas basins, Mars: Twins separated at birth. *J. Geophys. Res.* 111, doi:10.1029/2005JE002666. E08005.
- Simons, M., Solomon, S.C., Hager, B.H., 1997. Localization of gravity and topography: Constraints on the tectonics and mantle dynamics of Venus. *Geophys. J. Int.* 131, 24–31.
- Simpson, R.W., 1997. Quantifying Anderson's fault types. *J. Geophys. Res.* 102, 17909–17919.
- Smith, D.E., Sjogren, W.L., Tyler, G.L., Balmino, G., Lemoine, F.G., Konopliv, A.S., 1999a. The gravity field of Mars: Results from Mars Global Surveyor. *Science* 286, 94–97.
- Smith, D.E., Zuber, M.T., Solomon, S.C., Phillips, R.J., Head, J.W., Garvin, J.B., Banerdt, W.B., Muhleman, D.O., Pettengill, G.H., Neumann, G.A., Lemoine, F.G., Abshire, J.B., Aharonson, O., Brown, D.C., Hauck, S.A., Ivanov, A.B., McGovern, P.J., Zwally, H.J., Duxbury, T.C., 1999b. The global topography of Mars and implications for surface evolution. *Science* 284, 1495–1503.
- Smith, D.E., Zuber, M.T., Frey, H.V., Garvin, J.B., Head, J.W., Muhleman, D.O., Pettengill, G.H., Phillips, R.J., Solomon, S.C., Zwally, H.J., Banerdt, W.B., Duxbury, T.C., Golombek, M.P., Lemoine, F.G., Neumann, G.A., Rowlands, D.D., Aharonson, O., Ford, P.G., Ivanov, A.B., Johnson, C.L., McGovern, P.J., Abshire, J.B., Afzal, R.S., Sun, X., 2001. Mars Orbiter Laser Altimeter: Experiment summary after the first year of global mapping of Mars. *J. Geophys. Res.* 106, 23689–23722, doi:10.1029/2000JE001364.
- Solomon, S.C., Head, J.W., 1980. Lunar mascon basins—Lava filling, tectonics, and evolution of the lithosphere. *Rev. Geophys.* 18, 107–141.
- Solomon, S.C., Head, J.W., 1990. Heterogeneities in the thickness of the elastic lithosphere of Mars: Constraints on heat flow and internal dynamics. *J. Geophys. Res.* 95, 11073–11083.
- Spohn, T., Acuna, M.H., Breuer, D., Golombek, M., Greeley, R., Halliday, A., Hauber, E., Jaumann, R., Sohl, F., 2001. Geophysical constraints on the evolution of Mars. *Space Sci. Rev.* 96, 231–262.
- Tanaka, K., Skinner, J., Hare, T., 2005. Geologic map of the Northern Plains of Mars. U.S. Geol. Surv. Sci. Invest. Ser.
- Tornabene, L.L., Moersch, J.E., McSween Jr., H.Y., Hamilton, V.E., Piatek, J.L., Christensen, P.R., 2008. Surface and crater-exposed lithologic units of the Isidis Basin as mapped by coanalysis of THEMIS and TES derived data products. *J. Geophys. Res.* 113, doi:10.1029/2007JE002988. E10001.
- Turcotte, D.L., Willemann, R.J., Haxby, W.F., Norberry, J., 1981. Role of membrane stresses in the support of planetary topography. *J. Geophys. Res.* 86, 3951–3959.
- Tyler, G.L., Balmino, G., Hinson, D.P., Sjogren, W.L., Smith, D.E., Simpson, R.A., Asmar, S.W., Priest, P., Twicken, J.D., 2001. Radio science observations with Mars Global Surveyor: Orbit insertion through one Mars year in mapping orbit. *J. Geophys. Res.* 106, 23327–23348, doi:10.1029/2000JE001348.
- Wessel, P., Smith, W.H.F., 1998. New, improved version of Generic Mapping Tools released. *EOS Trans. AGU* 79, 579.
- Wichman, R.W., Schultz, P.H., 1989. Sequence and mechanisms of deformation around the Hellas and Isidis impact basins on Mars. *J. Geophys. Res.* 94, 17333–17357.
- Wieczorek, M.A., Phillips, R.J., 1998. Potential anomalies on a sphere: Applications to the thickness of the lunar crust. *J. Geophys. Res.* 103, 1715–1724.
- Wieczorek, M.A., Phillips, R.J., 1999. Lunar multiring basins and the cratering process. *Icarus* 139, 246–259, doi:10.1006/icar.1999.6102.
- Wieczorek, M.A., Simons, F.J., 2005. Localized spectral analysis on the sphere. *Geophys. J. Int.* 162, 655–675, doi:10.1111/j.1365-246X.2005.02687.x.
- Wieczorek, M.A., Zuber, M.T., 2004. Thickness of the martian crust: Improved constraints from geoid-to-topography ratios. *J. Geophys. Res.* 109, doi:10.1029/2003JE002153. E01009.
- Willemann, R.J., Turcotte, D.L., 1982. The role of lithospheric stress in the support of the Tharsis rise. *J. Geophys. Res.* 87, 9793–9801.
- Yuan, D.N., Sjogren, W.L., Konopliv, A.S., Kucinskis, A.B., 2001. Gravity field of Mars: A 75th degree and order model. *J. Geophys. Res.* 106, 23377–23402, doi:10.1029/2000JE001302.
- Zuber, M.T., Solomon, S.C., Phillips, R.J., Smith, D.E., Tyler, G.L., Aharonson, O., Balmino, G., Banerdt, W.B., Head, J.W., Johnson, C.L., Lemoine, F.G., McGovern, P.J., Neumann, G.A., Rowlands, D.D., Zhong, S., 2000. Internal structure and early thermal evolution of Mars Global Surveyor topography and gravity. *Science* 287, 1788–1793.